

Charge Density Waves as a Tool for Creating Idealized (Magnetic) Topological Semimetals

Shiming Lei,¹ Samuel M. L. Teicher,² Andreas Topp,³ Kehan Cai,¹ Jingjing Lin,⁴ Fanny Rodolakis,⁵ Jessica L. McChesney,⁵ Maxim Krivenkov,⁶ Dmitry Marchenko,⁶ Andrei Varykhalov,⁶ Christian R. Ast,³ Roberto Car,^{1,4} Jennifer Cano,^{7,8} Maia G. Vergniory,⁹ N. Phuan Ong,⁴ and Leslie M. Schoop^{1,*}

¹*Department of Chemistry, Princeton University,
Princeton, New Jersey 08544, USA*

²*Materials Department and Materials Research Laboratory,
University of California, Santa Barbara, California 93106, USA*

³*Max-Planck-Institut für Festkörperforschung, Stuttgart, 70569, Germany*

⁴*Department of Physics, Princeton University, Princeton, NJ 08544, USA*

⁵*Argonne National Laboratory, 9700 South Cass Avenue, Argonne, IL 60439, USA*

⁶*Helmholtz-Zentrum Berlin für Materialien und Energie,
Elektronenspeicherring BESSY II, Albert-Einstein-Straße 15, 12489 Berlin, Germany*

⁷*Department of Physics and Astronomy,
Stony Brook University, Stony Brook, New York 11974, USA*

⁸*Center for Computational Quantum Physics,
The Flatiron Institute, New York, New York 10010, USA*

⁹*Donostia International Physics Center, 20018 Donostia-San Sebastian,
Spain and IKERBASQUE, Basque Foundation for Science,
Maria Diaz de Haro 3, 48013 Bilbao, Spain*

(Dated: May 27, 2022)

Abstract

New developments in the field of topological matter are often driven by materials discovery. In the last few years, large efforts have been performed to classify all known inorganic materials with respect to their topology. Unfortunately, a large number of topological materials suffer from non-ideal band structures. For example, topological bands are frequently convoluted with trivial ones, and band structure features of interest can appear far below the Fermi level. This leaves just a handful of materials that are intensively studied. Finding strategies to design new topological materials is a solution. Here we introduce a new mechanism that is based on charge density waves and non-symmorphic symmetry to design an idealized topological semimetal. We then show experimentally that the antiferromagnetic compound $\text{GdSb}_{0.46}\text{Te}_{1.48}$ is a nearly ideal topological semimetal based on the proposed mechanism. Its highly unusual transport behavior points to a thus far unknown regime, in which Dirac carriers with Fermi energy very close to the node gradually localize in the presence of lattice and magnetic disorder.

Topological matter has fascinated the field of condensed matter physics in the last decade due to its potential for understanding properties of matter in a new way. Phenomena that have been discovered in topological materials include the quantum spin Hall effect (1, 2), quantum anomalous Hall effect (3), absence of back-scattering (4), ultrahigh carrier mobility and giant magnetoresistance (5–7), and topological Fermi arc states (8–11). While many topological materials have been discovered, there are only a handful that have been studied intensively (12–14). Recently, various algorithms have been developed to scan through a large number of known non-magnetic materials, which are then catalogued in databases with respect to their topological classification (15–17). While these efforts are a great help for gaining a general understanding about what kinds of materials are topological, coincidentally the “best” topological materials had already been discovered before. For example Sn-doped $(\text{Bi,Sb})_2\text{Te}_2\text{S}$ is still the topological insulator with the largest band gap (18) and graphene is still the topological semimetal (TSM) with the largest range of linear band dispersion (19). Common shortcomings of most topological materials are that their topologically relevant states are often below/above the Fermi level or that trivial states interfere with the relevant bands at the Fermi level. Furthermore, the materials search lags behind when it comes to magnetic materials, where only a few studies with limited examples exist (20, 21).

If viewed from a chemical perspective, topological band structures can be linked to delocalized chemical bonds, which often appear in compounds that are prone to undergo Peierls distortions (22, 23). For example, the Dirac cone in graphene is chemically stabilized by its delocalized, conjugated π -electrons. Although graphene features a half-filled band, which would indicate a propensity to a (charge density wave) CDW distortion, it keeps its hexagonal symmetry. Such behavior can be understood by considering graphene’s Fermi surface (FS), which only consists of isolated K and K’ points and thus disfavors the FS nesting condition of CDW formation. A different class of TSMs that features delocalized bonds are square-net materials. An example is the nodal-line semimetal ZrSiS, which features a dense Si square net with half-filled p_x - and p_y -bands (24, 25). The band structure features a diamond-shaped nodal line at the Fermi level, which will gap to a weak topological insulating state with high spin-orbit coupling (SOC), as well as four-fold degenerate Dirac nodes at the Brillouin zone (BZ) boundaries, which are robust against SOC (Fig. 1). The latter are a consequence of non-symmorphic symmetry, which was previously suggested as a mechanism to design Dirac semimetals in square nets by Young and Kane (26). For half-

filled p_x - and p_y -bands, the non-symmorphically-enforced Dirac crossing can appear at or near the Fermi level, depending on the strength of next-nearest-neighbor interactions in the square net (26, 27). A material with a “clean” (i.e. with no other interfering bands) non-symmorphically protected Dirac node at the Fermi level has not yet been achieved, to the best of our knowledge.

Square-net materials with the MXZ formula in space group $P4/nmm$ (isostructural to ZrSiS), are known to have large chemical flexibility and importantly, the M site is able to incorporate rare earth elements, thus providing an opportunity to study the effect of magnetism and potentially correlations on the topological band structure. In this context, $LnSbTe$ materials ($Ln =$ lanthanide) that are isostructural and isoelectronic to ZrSiS have been suggested as promising candidates (28–33). However, the band structure of these materials is not as “clean” as in ZrSiS: the FS contains trivial pockets, in addition to the nodal-line states.

It is well established that CDWs can be induced by chemical substitution in $LnSbTe$ systems (32, 34). Here, we show how these CDWs, in combination with non-symmorphic symmetry, can be utilized to design “clean” non-symmorphic TSMs: The CDW gaps out states within the BZ, while the non-symmorphic symmetry-enforced band crossings at the BZ boundary, which is at the Fermi level in $LnSb_xTe_{2-x}$ for certain values of x , is unaffected. Experimentally, we focus on $GdSb_{0.46}Te_{1.48}$ and show with angle-resolved photoemission spectroscopy (ARPES) that a non-symmorphically protected Dirac crossing appears at the Fermi level, with minimal interference from trivial bands. In addition, we reveal that $GdSb_{0.46}Te_{1.48}$ exhibits a very complex magnetic phase diagram and highly unusual transport properties.

Square-net materials, such as ZrSiS and GdSbTe, feature side-centered square nets as shown in Fig. 1A. Such nets are commonly referred to as 4^4 -nets in crystallography literature (35, 36). The atoms occupying the 4^4 -net (Si and Sb respectively) have six electrons, resulting in half-filled p_x - and p_y -orbitals. A tight-binding (TB) model of a two-dimensional 4^4 net of p_x - and p_y -orbitals, similar to that in refs. (23, 27), is thus considered. The resulting TB band structure is shown in Fig. 1B. Both the nodal line that defines the diamond-shaped FS (referred to as the *mirror-symmetry-protected* Dirac node (m-DN)), and the non-symmorphically enforced degeneracies at X and M (referred to as *non-symmorphically-protected* Dirac node (ns-DN)) are revealed in the model. When electrons are added to the

system, the FS will become nested (Fig. 1C). Therefore CDWs are expected to appear when adding electrons to the system. In accordance, CDWs have been reported in LaSe₂ (37), rare-earth ditellurides (34), and rare-earth tritellurides (38). Note that the CDW appears above room temperature in these systems. For a band filling of $E = E_2$ (Fig. 1B), the Fermi level crosses the ns-DN at X. In addition, the Fermi level crosses the m-Dirac nodal-line bands along Γ -X and Γ -M, but above the m-DN. With a CDW, these additional band crossings can be gapped at the Fermi level, ideally to just leave the ns-DN. To test this hypothesis, we extended the TB model to a superstructure reflecting the CDW.

Previously, we reported on the structural evolution of GdSb_xTe_{2-x- δ} (δ describes the vacancy concentration), with varying Sb composition x (32). The CDW wave vector q_{CDW} in GdSb_{0.46}Te_{1.48} was determined to be 0.20 r.l.u. (reciprocal lattice unit) and single crystal x-ray diffraction revealed that GdSb_{0.46}Te_{1.48} adopts a five-fold superstructure in the orthorhombic space group $Pm\bar{m}n$, in which the 4⁴-net forms zig-zag chains (Fig. 1D), retaining the non-symmorphic symmetry. The square net in the TB model was modeled with anisotropic nearest-neighbor-hopping parameters as well as by a five-fold increase of the unit cell in one direction (Fig. 1E, more details are given in Methods). To compare the resulting band structure with that of the subcell, the supercell band structure is unfolded into the subcell BZ (Fig. 1F, also see fig. S1). The Fermi level was set to $E = E_2$. Along Γ -X, there are now several ns-DNs that result from band folding, which appear with reduced spectral weight relative to the original one. The Fermi level cuts through the center of each of these ns-DNs. Along S- Γ , the bands that contribute to the m-DN also cross the Fermi level, because the band gaps created by the CDW appear slightly above E_F . However, depending on the intensity of the CDW modulation (which we have modeled by the strength of the differed hopping in the TB model), the Fermi level can reside within the gaps along S- Γ , as we will experimentally show below. Our TB model shows that a CDW will generally open gaps in the band structure, but the non-symmorphically-protected Dirac cones will be preserved, as long as the CDW preserves the non-symmorphic symmetry.

We now consider the real material system GdSb_xTe_{2-x- δ} . An illustration of the crystal structure of undistorted, tetragonal GdSbTe is shown in Fig. 1G and the corresponding DFT-calculated band structure is shown in Fig. 1I. Note that GdSbTe is modeled with the same orthorhombic lattice parameters as the subcell of GdSb_{0.46}Te_{1.48} and thereby the same $Pm\bar{m}n$ space group, to ease comparison. The BZ for a primitive orthorhombic cell

is shown in Fig. 1H. In the paramagnetic state, bands are guaranteed to be four-fold degenerate (counting spin) at the X, U, Y, T, S, and R points, respectively (for more details see Supplementary Materials).

Figure 1J shows an illustration of the ns-Dirac nodal line along X-U, which reveals a k_z dispersion. The ns-DN at X is 0.58 eV below that at U. Consequently, a Dirac crossing would appear at the FS as long as the Fermi level of $\text{GdSb}_x\text{Te}_{2-x-\delta}$ resides in between the energy span of X and U, which is indicated by the colored window in Fig. 1I. When the Fermi level resides in the blue-shaded region, it cuts through additional bands along Γ -X-S- Γ (marked by the arrows), resulting in a hole-pocket centered at Γ . Since an inclusion of a three-dimensional hole-pocket (see fig. S2) would impede CDW formation, the doping level x in $\text{GdSb}_x\text{Te}_{2-x-\delta}$ should be high enough to move the Fermi level to the green-shaded region, where this hole-pocket disappears. In this work, we choose $\text{GdSb}_{0.46}\text{Te}_{1.48}$ as the focus, where the Fermi level lies in the green region and a CDW, which preserves the non-symmorphic symmetry, has been reported to exist above room temperature.

We performed ARPES measurements on $\text{GdSb}_{0.46}\text{Te}_{1.48}$ single crystals to verify the proposed mechanism. A polarized optical image of one such crystal is shown in Fig. 2B. Figure 2A shows a selection of constant energy cuts from $E_F - 0.5$ eV to E_F , measured with a photon energy of $\hbar\omega = 70$ eV. We deduced this photon energy to correspond to the $k_z \approx \pi/c$ plane (for photon energy dependent data see fig. S3). The constant energy cut of 0.1 eV below E_F (Fig. 2A) reveals shadow bands near U and T. In contrast, the FS (Fig. 2C) only shows enhanced intensity at U and T, and very weak intensity close to U, which reflects the diamond-shaped FS (fig. S1C). Note that ARPES measurements are known to have a direct connection to the unfolded band structure, particularly for systems with enlarged cells with weak translational symmetry breaking, as is in the case of $\text{GdSb}_{0.46}\text{Te}_{1.48}$ (39, 40). The spectral weight of the shadow bands reflects the strength of their coupling to the broken translational symmetry of the normal cell (in this case, the five-fold CDW distortion).

To analyze the ARPES data, we performed DFT calculations on the superstructure, and unfolded the band structure to the subcell BZ (39) to allow a direct comparison with the measurements. Figure 2E and 2F show the measured band dispersion along $\bar{\Gamma}$ - \bar{X} - $\bar{\Gamma}$, which is parallel to the CDW direction. The Z-U-Z cut (Fig. 2E) measured with a photon energy of $\hbar\omega = 70$ eV shows a ns-Dirac crossing at U, with no other states interfering at the Fermi level. The overall band feature agrees with the DFT band dispersion in the

$k_z = \pi/c$ plane (Fig. 2H). Figure 2F shows ARPES data measured at a photon energy of $\hbar\omega = 100$ eV, which corresponds to the band dispersion along Γ Z-XU- Γ Z at $k_z = 0.6\pi/c$ (fig. S3). A corresponding Laplacian plot (41), $\nabla^2 f = \frac{\partial^2 f}{\partial^2 x} + \frac{\partial^2 f}{\partial^2 y}$, where f represents the measured ARPES intensity, and x and y represent the variables in k - and energy-space, respectively, is shown in Fig. 2G. In agreement with DFT, the ns-DN lowers in energy moving from U to X along k_z . The measured ns-DN ($k_x = -\pi/a$, $k_y = 0$ and $k_z = 0.6\pi/c$) is at $E_i = -0.34$ eV, compared to $E_i = -0.21$ eV in the DFT calculation (Fig. 2I). The calculated band dispersion along Γ -X- Γ ($k_z = 0$ plane) is shown in Fig. 2J. Here the ns-DN at X appears at $E_i = -0.66$ eV below the Fermi level. This indicates that the Dirac nodal line persists along the X-U line. If we compare the band structure of the supercell to that of the subcell ($\bar{\Gamma}$ - \bar{X} - $\bar{\Gamma}$ in Fig. 2D; for a more detailed comparison along all high-symmetry k -paths between subcell and supercell calculations, see fig. S4), it becomes evident that bands contributing to the nodal line along X-U are not affected by the CDW, while the additional bands crossing the Fermi level along $\bar{\Gamma}$ - \bar{X} are gapped.

We expect an in-plane anisotropy in the band structure due to the CDW, which is visible in the ARPES measurements. Figure 3A shows the ARPES band dispersion as well as its Laplacian (Fig. 3B) along the Z-T-Z direction, perpendicular to the previous cut. The ns-DN at T is 0.29 eV below the Fermi level, in contrast to near-Fermi-level ns-DN at U (Fig. 2F). The experimentally measured band anisotropy is in qualitative, albeit not exact agreement with that from DFT, where the DN at T appears only 0.09 eV below the Fermi level (Fig. 3C). This discrepancy could be related to the existence of twinning in the crystals (see Sample Synthesis in Methods).

Data for the diagonal cut along the RS-Z Γ -RS plane is shown in Fig. 3. Here, the CDW also gaps states at the Fermi level. The band dispersion plots measured with $\hbar\omega = 100$ eV are shown in Fig. 3, D (1st BZ) and G (2nd BZ) (data taken at $\hbar\omega = 70$ eV can be found in fig. S5 in the Supplementary Materials). Figure 3, E and H, shows their Laplacian plots, respectively. At the Fermi level, the band intensity is significantly weakened. The DFT calculation (Fig. 3F) reveals the cause for this weakening effect: The CDW opens a gap along the SR- Γ Z-SR plane in BZ and the actual Fermi level is very close to the band edge (Fig. 3F). At 0.62 eV below the Fermi level, the m-Dirac line nodes are visible in the DFT calculations. In the ARPES measurement, however, this crossing seems to be gapped by SOC, which appears at around 0.41 eV below E_F (Fig. 3H, indicated by black arrows).

Comparing the two diagonal cuts in the 1st BZ and 2nd BZ, the latter is in good agreement with the DFT calculation, but for the former, a branch of the m-Dirac bands is missing (marked by dashed line). This phenomenon might be related to a matrix element effect (42). The overall agreement between DFT and ARPES is high, albeit some disagreements in energy, which could be related to band renormalization due to correlation effects, which are not considered in the calculations, or other common inaccuracies of PBE-DFT. Such correlations could arise due to magnetic moments in the compounds or due to its nodal line structure, as correlations have been observed in the nonmagnetic square-net systems, ZrSiS (43) and ZrSiSe (44).

Finally, we would like to point out that in TSMs that result from non-symmorphic symmetry such as ZrSiS, surface floating bands are expected to occur due to a reduced symmetry at the surface (45). Thus the question whether such surface floating bands are observed in $\text{GdSb}_{0.46}\text{Te}_{1.48}$ naturally arises. As we show in fig. S6, we observe surface states along $\bar{Y} - \bar{S} - \bar{Y}$, which is the same direction floating bands are commonly observed as in other square net materials (45).

We also report the transport and magnetic properties of $\text{GdSb}_{0.46}\text{Te}_{1.48}$. The temperature dependent resistivity, measured on a single crystal of $\text{GdSb}_{0.46}\text{Te}_{1.48}$ is shown in Fig. 4A. The resistivity increases as the temperature decreases, despite the non-zero density of states at the Fermi level. This is in stark contrast to the structurally related rare-earth tri-tellurides, which are very good metals with extremely high mobility (46). The resistivity of $\text{GdSb}_{0.46}\text{Te}_{1.48}$ does not follow the classic activated behaviour expected for semiconductors (fig. S7A). It can rather be described by a power-law relation $\rho = \rho_0 T^{-0.29}$ (ρ increases by a factor of 5 as the temperature T decreases from 300 to 1.8 K). This is perhaps the most interesting electronic property observed in $\text{GdSb}_{0.46}\text{Te}_{1.48}$. First, because the Hall effect reveals that the increase in ρ is not mainly due to a decrease of the carrier density (fig. S7, C and D), we infer that the gradual power-law increase reflects gradual localization of the carriers. However, this localization behavior seems incompatible with the standard picture of weak (Anderson) localization in either 2D or 3D. Anderson localization (47) occurs when the carrier's diffusion length $\ell = \sqrt{D\tau_{in}}$ extends over a macroscopic distance of about 1 μm (D is the diffusion constant and τ_{in} the inelastic lifetime determined by electron-phonon scattering). Within the coherent area ℓ^2 free from phonon scattering, constructive interference between two paths of a wave packet that are time-reversed partners leads to localization

of the wave packet. Hence weak localization typically onsets at cryogenic temperatures or lower. By contrast, we observe a robust power law that extends to 300 K. At such warm temperatures, very strong phonon scattering renders $\tau_{in} < \tau$ (τ is the elastic scattering time), so that localization effects should not be observable. The magnetoresistance (MR) also strongly disagrees with weak localization. In Anderson localization, the resistivity increase observed at low T is highly sensitive to suppression by a weak external magnetic field H (the suppression is isotropic in 3D). The negative MR results from the destruction of the constructive interference within the coherent area. Complete suppression occurs when H inserts a flux quantum ϕ_0 within the coherent patch. By contrast, the resistivity profile here is nearly insensitive to external H . In a 1 T field, ρ increases, but only by 1.4% at 1.7 K (fig. S7B). We tentatively propose that the unusual situation of having isolated Dirac nodes in the presence of CDWs, lattice disorder, and complex magnetic phases (as we show below) creates a new situation that has not yet been accessed experimentally. Further investigation of this regime is ongoing.

The carrier type and mobility was extracted with a two-band model fit to the Hall resistivity (Fig. 4B). The hole and electron concentration is estimated to be $n_h = 8.3 \times 10^{18} \text{ cm}^{-3}$ and $n_e = 3.7 \times 10^{16} \text{ cm}^{-3}$, respectively. Their mobility is $21 \text{ cm}^2 \text{ V}^{-1} \text{ s}^{-1}$ and $284 \text{ cm}^2 \text{ V}^{-1} \text{ s}^{-1}$ at 3 K, respectively. For comparison, similar transport measurements were performed on a tetragonal analogue, $\text{GdSb}_{0.85}\text{Te}_{1.15}$, where no CDW distortion occurs. The resistivity displays metallic behavior until Néel temperature of $T_N \approx 12 \text{ K}$ (fig. S8). The carrier concentration is $n_e = 2.5 \times 10^{21} \text{ cm}^{-3}$, with electrons as the dominant carrier type. Clearly, $\text{GdSb}_{0.46}\text{Te}_{1.48}$ possesses significantly fewer carriers, which is a logical consequence of the CDW.

Figure 4C shows the magnetic susceptibility map of $\text{GdSb}_{0.46}\text{Te}_{1.48}$ in the parameter space of field and temperature. Three magnetically ordered phases are visible. Under a small field of 0.01 T, the highest transition appears at $T_N = 13.2 \text{ K}$, followed by a second transition at $T_1 = 8.5 \text{ K}$, and third transition at $T_2 = 7.2 \text{ K}$. When the magnetic field increases, the window between T_1 and T_2 shrinks and eventually disappears at a critical field of 1.1 T. Above this field, only two transitions exist up to 9 T. Overall, three magnetically ordered phases exist. Figure 4D shows an illustration of the magnetic phase diagram. Such a complex magnetic phase diagram is in sharp contrast to that of tetragonal $\text{GdSb}_{0.85}\text{Te}_{1.15}$, where only one magnetic transition was reported (32).

In summary, we introduced a new mechanism to design idealized topological semimetals that is based on the cooperative effect of a CDW and non-symmorphic symmetry. The proposed mechanism is experimentally demonstrated in $\text{GdSb}_{0.46}\text{Te}_{1.48}$, showing that the band structure is composed of Dirac nodes at the Fermi level, with minimal interference of other states. Finally, we show that $\text{GdSb}_{0.46}\text{Te}_{1.48}$ possesses exotic transport behavior and complex magnetism. Arguably, the most interesting feature is the robust power-law increase in the resistivity which onsets near room temperature. From the high-temperature onset and the absence of significant MR, this “localization” effect does not follow the usual paradigm of Anderson localization. The unusual situation of having isolated Dirac nodes in the presence of strong magnetic disorder realizes a new transport regime deserving of further investigation.

The appearance of complex magnetism, CDWs, and topological Dirac states, as well as their overlap, in one material system is of great interest for future studies. This is in analogy to the interplay of structural, magnetic, and electronic degrees of freedom, that has long been the subject of study on high-temperature superconductors, such as $\text{La}_{1.6-x}\text{Nd}_{0.4}\text{Sr}_x\text{CuO}_4$ (48) and $\text{La}_{2-x}\text{Ba}_x\text{CuO}_4$ (49). We note that the study of this interplay of magnetism, CDW, and Dirac states is not limited to the $\text{GdSb}_x\text{Te}_{2-x-\delta}$ system. The CDW instability is expected for electron-rich, layered square-net materials in general, that comply with the electron counting rules established by Papoian and Hoffmann (50). Therefore, our proposed mechanism can be considered as a general mechanism to design an idealized TSMs in this category of materials. In the $\text{LnSb}_x\text{Te}_{2-x-\delta}$ family, the essential requirement is the preservation of the non-symmorphic symmetry in the superstructure. We would like to note that incommensurate CDWs might also be able to preserve the Dirac nodes at the BZ boundary, while reducing additional band crossings at the Fermi level. Further studies are needed to elucidate this possibility. In this work, we did not yet analyze the role of magnetism on the band structure. Depending on the orientation of the spins, the electronic structure can be modified. Magnetism can be an additional way to tune the material properties, as has been reported for CeSbTe before (28).

* lschoop@princeton.edu

[1] B. A. Bernevig, T. L. Hughes, and S.-C. Zhang, *Science* **314**, 1757 (2006).

- [2] M. König, S. Wiedmann, C. Brüne, A. Roth, H. Buhmann, L. W. Molenkamp, X.-L. Qi, and S.-C. Zhang, *Science* **318**, 766 (2007).
- [3] C. Z. Chang, J. Zhang, X. Feng, J. Shen, Z. Zhang, M. Guo, K. Li, Y. Ou, P. Wei, L. L. Wang, Z. Ji, Y. Feng, S. Ji, X. Chen, J. Jia, X. Dai, Z. Fang, S. C. Zhang, K. He, Y. Wang, L. Lu, X. C. Ma, and Q. K. Xue, *Science* **340**, 167 (2013).
- [4] X.-L. Qi and S.-C. Zhang, *Reviews of Modern Physics* **83**, 1057 (2011).
- [5] T. Liang, Q. D. Gibson, M. N. Ali, M. Liu, R. J. Cava, and N. P. Ong, *Nature Materials* **14**, 280 (2015).
- [6] C. Shekhar, A. K. Nayak, Y. Sun, M. Schmidt, M. Nicklas, I. Leermakers, U. Zeitler, Y. Skourski, J. Wosnitza, Z. Liu, Y. Chen, W. Schnelle, H. Borrmann, Y. Grin, C. Felser, and B. Yan, *Nature Physics* **11**, 645 (2015).
- [7] M. N. Ali, J. Xiong, S. Flynn, J. Tao, Q. D. Gibson, L. M. Schoop, T. Liang, N. Hal-
dolaarachchige, M. Hirschberger, N. P. Ong, and R. J. Cava, *Nature* **514**, 205 (2014).
- [8] S. Y. Xu, I. Belopolski, N. Alidoust, M. Neupane, G. Bian, C. Zhang, R. Sankar, G. Chang, Z. Yuan, C. C. Lee, S. M. Hunag, H. Zheng, J. Ma, D. S. Sanchez, B. K. Wang, A. Bansil, F. Chou, P. P. Shibayev, H. Lin, S. Jai, and M. Z. Hasan, *Science* **349**, 613 (2015).
- [9] B. Q. Lv, H. M. Weng, B. B. Fu, X. P. Wang, H. Miao, J. Ma, P. Richard, X. C. Huang, L. X. Zhao, G. F. Chen, F. Fang, Z. Dai, T. Qian, and H. Ding, *Phys. Rev. X* **5**, 031013 (2015).
- [10] B. Q. Lv, N. Xu, H. M. Weng, J. Z. Ma, P. Richard, X. C. Huang, L. X. Zhao, G. F. Chen, C. Matt, F. Bisti, V. N. Strocov, J. Mesot, Z. Fang, X. Dai, T. Qian, M. Shi, and H. Ding, *Nature Physics* **11**, 724 (2015).
- [11] L. X. Yang, Z. K. Liu, Y. Sun, H. Peng, H. F. Yang, T. Zhang, B. Zhou, Y. Zhang, Y. F. Guo, M. Rahn, D. Prabhakaran, Z. Hussain, S.-K. Mo, C. Felser, B. Yan, and Y. L. Chen, *Nature Physics* **11**, 728 (2015).
- [12] B. Yan and C. Felser, *Annual Review of Condensed Matter Physics* **8**, 337 (2017).
- [13] N. Armitage, E. Mele, and A. Vishwanath, *Reviews of Modern Physics* **90**, 015001 (2018).
- [14] Y. Tokura, K. Yasuda, and A. Tsukazaki, *Nature Reviews Physics* **1**, 126 (2019).
- [15] F. Tang, H. C. Po, A. Vishwanath, and X. Wan, *Nature* **566**, 486 (2019).
- [16] M. Vergniory, L. Elcoro, C. Felser, N. Regnault, B. A. Bernevig, and Z. Wang, *Nature* **566**, 480 (2019).
- [17] T. Zhang, Y. Jiang, Z. Song, H. Huang, Y. He, Z. Fang, H. Weng, and C. Fang, *Nature* **566**,

- 475 (2019).
- [18] S. Kushwaha, I. Pletikosić, T. Liang, A. Gyenis, S. Lapidus, Y. Tian, H. Zhao, K. Burch, J. Lin, W. Wang, H. Ji, A. V. Fedorov, A. Yazdani, N. P. Ong, T. Valla, and R. J. Cava, *Nature Communications* **7**, 1 (2016).
 - [19] A. C. Neto, F. Guinea, N. M. Peres, K. S. Novoselov, and A. K. Geim, *Reviews of Modern Physics* **81**, 109 (2009).
 - [20] Y. Xu, L. Elcoro, Z. Song, B. J. Wieder, M. Vergniory, N. Regnault, Y. Chen, C. Felser, and B. A. Bernevig, arXiv:2003.00012 (2020).
 - [21] J.-R. Soh, F. De Juan, M. G. Vergniory, N. B. M. Schröter, M. C. Rahn, D. Y. Yan, J. Jiang, M. Bristow, P. A. Reiss, J. N. Blandy, Y. F. Guo, Y. G. Shi, T. K. Kim, A. McCollam, S. H. Simon, Y. Chen, A. I. Coldea, and A. T. Boothroyd, *Physical Review B* **100**, 201102 (2019).
 - [22] L. M. Schoop, F. Pielhofer, and B. V. Lotsch, *Chemistry of Materials* **30**, 3155 (2018).
 - [23] S. Klemenz, A. K. Hay, S. M. L. Teicher, A. Topp, J. Cano, and L. M. Schoop, *Journal of the American Chemical Society* **142**, 6350 (2020).
 - [24] L. M. Schoop, M. N. Ali, C. Straßer, A. Topp, A. Varykhalov, D. Marchenko, V. Duppel, S. S. Parkin, B. V. Lotsch, and C. R. Ast, *Nature Communications* **7**, 1 (2016).
 - [25] S. Klemenz, S. Lei, and L. M. Schoop, *Annual Review of Materials Research* **49**, 185 (2019).
 - [26] S. M. Young and C. L. Kane, *Phys. Rev. Lett.* **115**, 126803 (2015).
 - [27] S. Klemenz, L. Schoop, and J. Cano, *Phys. Rev. B* **101**, 165121 (2020).
 - [28] L. M. Schoop, A. Topp, J. Lippmann, F. Orlandi, L. Mühler, M. G. Vergniory, Y. Sun, A. W. Rost, V. Duppel, M. Krivenkov, S. Sheoran, P. Manuel, A. Varykhalov, B. Yan, R. K. Kremer, C. R. Ast, and B. V. Lotsch, *Science Advances* **4**, eaar2317 (2018).
 - [29] A. Topp, M. G. Vergniory, M. Krivenkov, A. Varykhalov, F. Rodolakis, J. McChesney, B. V. Lotsch, C. R. Ast, and L. M. Schoop, *J. Phys. Chem. Solids* **128**, 296 (2019).
 - [30] M. M. Hosen, G. Dhakal, K. Dimitri, P. Maldonado, A. Aperis, F. Kabir, C. Sims, P. Riseborough, P. M. Oppeneer, D. Kaczorowski, T. Durakiewicz, and M. Neupane, *Scientific Reports* **8**, 13283 (2018).
 - [31] R. Sankar, I. P. Muthuselvam, K. R. Babu, G. S. Murugan, K. Rajagopal, R. Kumar, T.-C. Wu, C.-Y. Wen, W.-L. Lee, G.-Y. Guo, and F.-C. Chou, *Inorganic Chemistry* **58**, 11730 (2019).
 - [32] S. Lei, V. Duppel, J. M. Lippmann, J. Nuss, B. V. Lotsch, and L. M. Schoop, *Advanced Quantum Technologies* **2**, 1900045 (2019).

- [33] A. Weiland, D. G. Chaparro, M. G. Vergniory, E. Derunova, J. Yoon, I. W. Oswald, G. T. McCandless, M. Ali, and J. Y. Chan, *APL Materials* **7**, 101113 (2019).
- [34] E. DiMasi, B. Foran, M. C. Aronson, and S. Lee, *Phys. Rev. B* **54**, 13587 (1996).
- [35] W. Tremel and R. Hoffmann, *J. Am. Chem. Soc.* **109**, 124 (1987).
- [36] J. Nuss, U. Wedig, and M. Jansen, *Z. Kristallogr. Cryst. Mater.* **221**, 554 (2006).
- [37] S. Bénazeth, D. Carré, and P. Laruelle, *Acta Crystallographica Section B: Structural Crystallography and Crystal Chemistry* **38**, 33 (1982).
- [38] E. DiMasi, M. C. Aronson, J. F. Mansfield, B. Foran, and S. Lee, *Phys. Rev. B* **52**, 14516 (1995).
- [39] W. Ku, T. Berlijn, and C.-C. Lee, *Physical Review Letters* **104**, 216401 (2010).
- [40] E. van Heumen, J. Vuorinen, K. Koepernik, F. Masee, Y. Huang, M. Shi, J. Klei, J. Goedkoop, M. Lindroos, J. van den Brink, and M. S. Golden, *Physical Review Letters* **106**, 027002 (2011).
- [41] P. Zhang, P. Richard, T. Qian, Y.-M. Xu, X. Dai, and H. Ding, *Review of Scientific Instruments* **82**, 043712 (2011).
- [42] D. Inosov, J. Fink, A. Kordyuk, S. Borisenko, V. Zabolotnyy, R. Schuster, M. Knupfer, B. Büchner, R. Follath, H. Dürr, W. Eberhardt, V. Hinkov, B. Keimer, and H. Berger, *Physical Review Letters* **99**, 237002 (2007).
- [43] S. Pezzini, M. R. van Delft, L. M. Schoop, B. V. Lotsch, A. Carrington, M. I. Katsnelson, N. E. Hussey, and S. Wiedmann, *Nature Physics* **14**, 178 (2018).
- [44] Y. Shao, A. Rudenko, J. Hu, Z. Sun, Y. Zhu, S. Moon, A. Millis, S. Yuan, A. Lichtenstein, D. Smirnov, Z. Q. Mao, M. I. Katsnelson, and D. N. Basov, *Nature Physics*, 1 (2020).
- [45] A. Topp, R. Queiroz, A. Grüneis, L. MÜchler, A. Rost, A. Varykhalov, D. Marchenko, M. Krivenkov, F. Rodolakis, J. McChesney, L. B. V, S. L. M, and C. R. Ast, *Phys. Rev. X* **7**, 041073 (2017).
- [46] S. Lei, J. Lin, Y. Jia, M. Gray, A. Topp, G. Farahi, S. Klemenz, T. Gao, F. Rodolakis, J. L. McChesney, C. R. Ast, A. Yazdani, K. S. Burch, S. Wu, N. P. Ong, and L. M. Schoop, *Science Advances* **6**, eaay6407 (2020).
- [47] P. A. Lee and T. Ramakrishnan, *Reviews of Modern Physics* **57**, 287 (1985).
- [48] J. Tranquada, B. Sternlieb, J. Axe, Y. Nakamura, and S. Uchida, *Nature* **375**, 561 (1995).
- [49] P. Abbamonte, A. Rusydi, S. Smadici, G. Gu, G. Sawatzky, and D. Feng, *Nature Physics* **1**, 155 (2005).

[50] A. G. Papoian and R. Hoffmann, *Angew. Chem. Int. Ed.* **39**, 2408 (2000).

ACKNOWLEDGMENTS

This research was supported by the Arnold and Mabel Beckman Foundation through a Beckman Young Investigator grant awarded to L.M.S. The authors acknowledge the use of Princeton’s Imaging and Analysis Center, which is partially supported by the Princeton Center for Complex Materials, a National Science Foundation (NSF)-MRSEC program (DMR-1420541). This research used resources of the Advanced Photon Source, a U.S. Department of Energy (DOE) Office of Science User Facility operated for the DOE Office of Science by Argonne National Laboratory under Contract No. DE-AC02-06CH11357. The work at UC Santa Barbara was supported by the National Science Foundation through the Q-AMASE-i Quantum Foundry, (DMR-1906325). We acknowledge use of the shared computing facilities of the Center for Scientific Computing at UC Santa Barbara, supported by NSF CNS-1725797, and the NSF MRSEC at UC Santa Barbara, NSF DMR-1720256. S.M.L.T. has been supported by the National Science Foundation Graduate Research Fellowship Program under Grant no. DGE-1650114. A.T. was supported by the DFG, proposal No. SCHO 1730/1-1. We thank HZB for the allocation of synchrotron radiation beamtime. M.K., D.M. and A.V. acknowledge support by the Impuls- und Vernetzungsfonds der Helmholtz-Gemeinschaft under grants No. HRJRG-408 and HRSF-0067 (Helmholtz-Russia Joint Research Groups). J.C. acknowledges the support of The Flatiron Institute, a division of the Simons Foundation. Any opinions, findings, and conclusions or recommendations expressed in this material are those of the authors and do not necessarily reflect the views of the National Science Foundation.

AUTHOR CONTRIBUTION

S.L. and L.M.S. conceived the project. S.L. grew the crystals and performed the magnetic measurements. S.M.L.T. calculated DFT electronic structures, with input from M.G.V. and L.M.S.. M.G.V. performed surface band calculations. S.L. and J.L. performed the transport measurements and analyzed the data with input from N.P.O. and L.M.S.. K.C. performed the tight-binding model calculation with input from J.C. S.L., L.M.S. and R.C.. S.L., A.T.,

F.R. and J.L.M. performed the core-level photoemission spectrum measurement at Argonne. A.T., A.V., M.K. and D.M. performed the ARPES measurements at BESSY. S.L., A.T. and L.M.S. analyzed and interpreted the results, with input from A.V., C.R.A., M.K. and D.M.. M.G.V. and J.C. performed the symmetry analysis. All authors discussed the results and contributed to writing the manuscript.

COMPETING INTERESTS

The authors declare no competing interests.

DATA AVAILABILITY

The data that support the findings of this study are available from the corresponding author upon reasonable request.

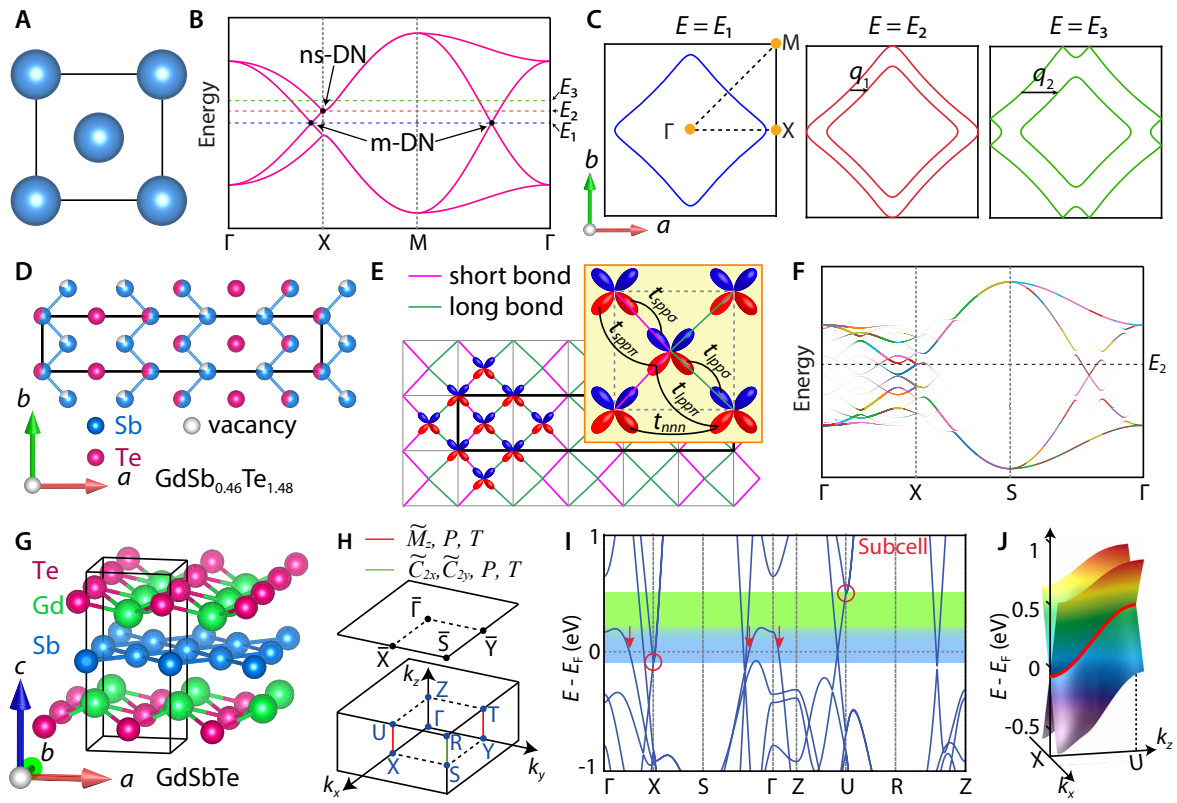


Fig. 1. Electronic structure of GdSbTe and the effect of CDWs in combination with non-symmorphic symmetry. (A) Illustration of a 4^4 -net lattice. (B) Band structure for a four-band TB model. E_1 , E_2 , and E_3 represent Fermi levels with three different band-fillings; E_1 corresponds to half filling, E_2 cuts right through the four-fold band degeneracy at X, and $E_3 = 2E_2 - E_1$, the ns-DN and m-DNs are indicated. (C) Fermi surface plots corresponding to the Fermi level at E_1 , E_2 , and E_3 . q_1 and q_2 represent the CDW nesting vectors. (D) Top view of the distorted square-net lattice forming a five-fold supercell in $\text{GdSb}_{0.46}\text{Te}_{1.48}$, with Te partial substitution of Sb, and the square net forming a chain-like texture. This illustrated supercell pattern is determined from single crystal diffraction (32). (E) Illustration of the TB model accounting for the five-fold superstructure, with p_x and p_y -orbitals on each site. The short and long bonds are colored in purple and green, respectively. The top-right inset illustrates the definition of the 5 hopping parameters that are considered in the TB model. (F) The calculated band structure from the superstructural TB model. E_F is set so that it cuts through the ns-DN at X. Different bands from the supercell are illustrated in different colors. (G) An illustration of the crystal structure of stoichiometric GdSbTe, which highlights the Sb 4^4 -net. (H) An illustration of the BZ for space group $Pmmn$. The lines where four-fold degeneracy is enforced (in the presence of SOC) by a combination of a non-symmorphic and time-reversal symmetry are indicated. The top plane shows the (001) surface BZ. (I) DFT-bulk band structure of stoichiometric GdSbTe without SOC. The energy span of the ns-Dirac line node along X-U is indicated by the colored window; the two endpoints at X and U are circled. The arrows indicate the trivial bands that cross the Fermi level, resulting in a hole-pocket at the FS for GdSbTe. For doped $\text{GdSb}_x\text{Te}_{2-x-\delta}$, this hole-pocket vanishes when the Fermi level lies within the green-shaded regime. (J) Illustration of the ns-Dirac nodal line (colored in red) along X-U.

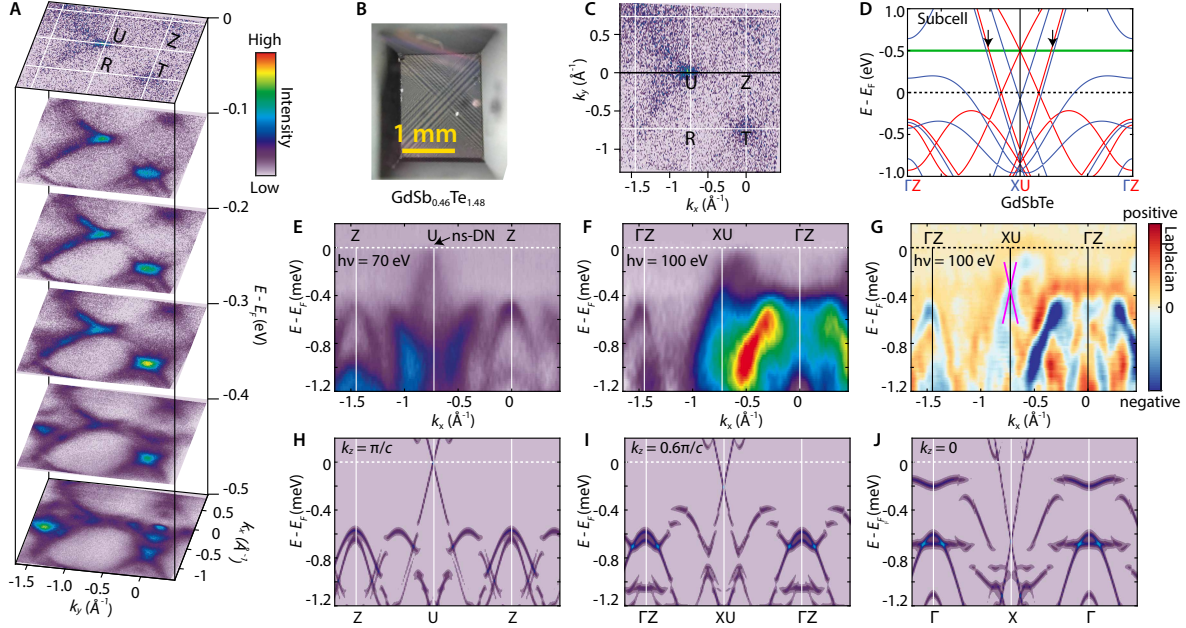


Fig. 2. ARPES data taken at $\hbar\omega = 70$ and 100 eV, in comparison to DFT calculations.

(A) Constant energy plots at various initial state energies ranging from -0.5 to 0 eV, measured with a photon energy of $\hbar\omega = 70$ eV. Shadow bands are visible at lower binding energies. (B) A polarized optical image of a plate-like $\text{GdSb}_{0.46}\text{Te}_{1.48}$ crystal. (C) Fermi surface measured at $\hbar\omega = 70$ eV. The black solid line indicates the line-path for band dispersion cut shown in (E). (D) DFT band dispersion for the undistorted subcell along Γ -X- Γ overlapped with that along Z-U-Z. Arrows indicate the bands that are gapped by the CDW. Note that the green line is set to cut through the ns-DN at U, indicating the adjusted Fermi level of $\text{GdSb}_{0.46}\text{Te}_{1.48}$ for a direct comparison with the supercell DFT band structure in (H). (E) Measured band dispersion along the Z-U-Z direction. The ns-DN at U is marked by the arrow. (F) Measured band dispersion along the Γ Z-XU- Γ Z ($k_z = 0.6\pi/c$ plane) direction. (G) Laplacian of the ARPES intensity plot shown in (F). Positive and negative Laplacians are a consequence of the minima and maxima, respectively. The Dirac crossing is marked by the purple lines, in comparison to the prediction in (I). (H to J) DFT calculated band dispersion corresponding to $k_z = \pi/c$, $k_z = 0.6\pi/c$ and $k_z = 0$ planes, respectively.

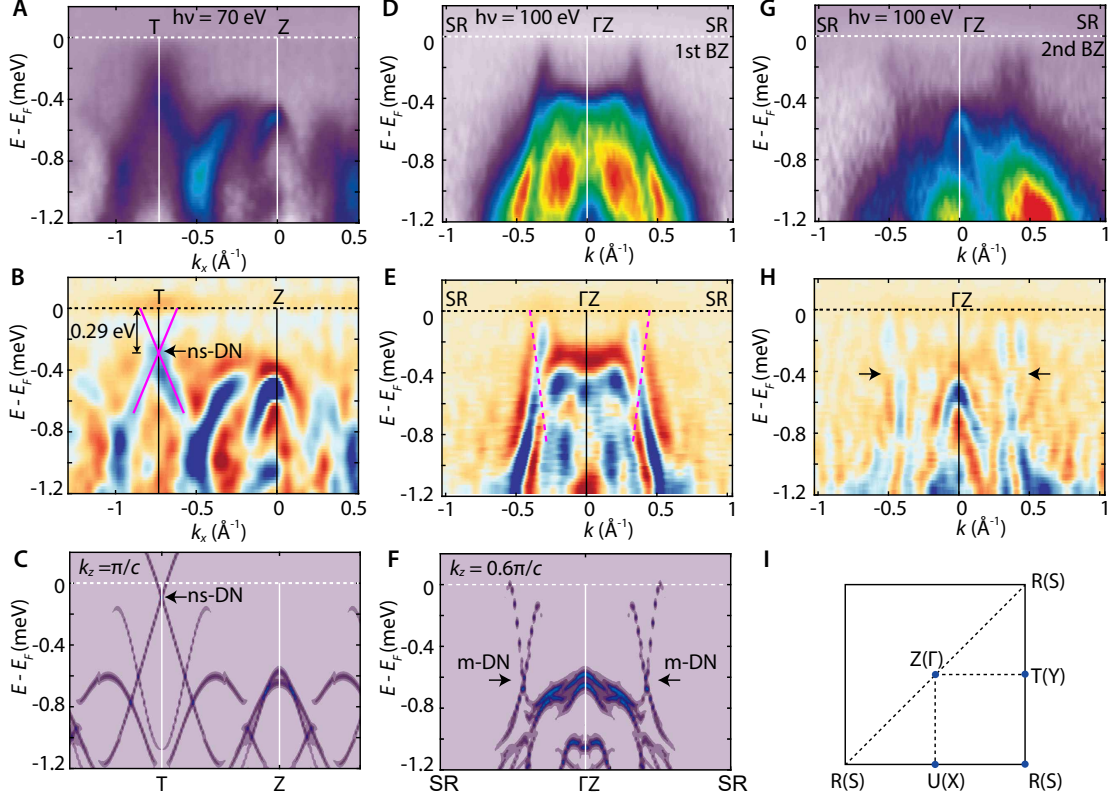


Fig. 3. Band dispersion of $\text{GdSb}_{0.46}\text{Te}_{1.48}$ along further high-symmetry paths. (A) ARPES intensity plot of the measured band dispersion along the Z-T-Z direction. (B) Laplacian of the ARPES intensity plot shown in (A). The Dirac crossing is indicated by the purple lines, with the ns-DN at $E_i = -0.29$ eV. (C) DFT calculated band dispersion at $k_z = \pi/c$. The DN is 0.09 eV below E_F . (D and G) ARPES intensity plot of the measured band dispersion along the UR- Γ Z-UR direction ($k_z = 0.6\pi/c$ plane) in the 1st BZ and 2nd BZ, respectively. (E and H) Laplacian of the ARPES intensity plots shown in (D) and (G), respectively. Arrows in (H) suggest the gapping of m-Dirac crossing due to SOC. The dashed purple lines in e indicate bands that are not clearly visualized in the 1st BZ, compared to that in 2nd BZ and the theoretical prediction in (F). (F) DFT calculated band dispersion along SR- Γ Z-SR ($k_z = 0.6\pi/c$) (without SOC). Arrows indicate the m-DNs. (I) Top view of the BZ in the planes of Z-U-R-T and Γ -X-S-Y.

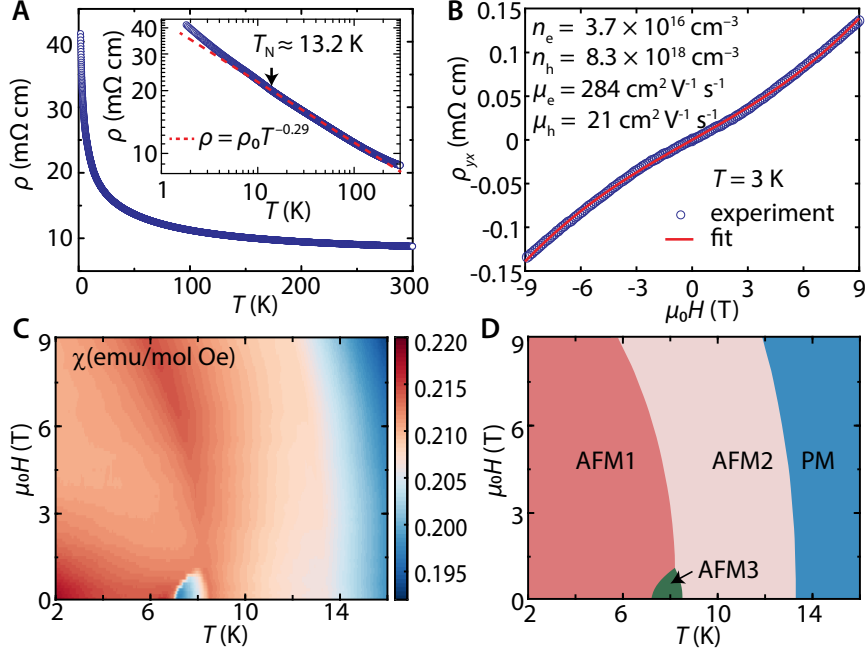


Fig. 4. Transport and magnetic properties of $\text{GdSb}_{0.46}\text{Te}_{1.48}$. (A) Temperature dependent resistivity, with no magnetic field applied. Inset shows the same data in a log-log plot. The dashed line shows a fit to a power-law in regime above the Néel temperature, $T_N = 13.2$ K. (B) Hall resistivity measured at 3 K; the carrier concentration and mobility from a two-band model fit are given. (C) Map of the DC magnetic susceptibility in the parameter space of magnetic field and temperature. (D) Illustration of the magnetic phase diagram inferred from the DC magnetic susceptibility map in (C). AFM1, AFM2, and AFM3 indicate three different types of antiferromagnetic phases, while PM indicates the paramagnetic phase.

Supplementary Materials for “Charge Density Waves as a Tool for Creating Idealized (Magnetic) Topological Semimetals”

Shiming Lei,¹ Samuel M. L. Teicher,² Andreas Topp,³ Kehan Cai,¹ Jingjing Lin,⁴ Fanny Rodolakis,⁵ Jessica L. McChesney,⁵ Maxim Krivenkov,⁶ Dmitry Marchenko,⁶ Andrei Varykhalov,⁶ Christian R. Ast,³ Roberto Car,^{1,4} Jennifer Cano,^{7,8} Maia G. Vergniory,⁹ N. Phuan Ong,⁴ and Leslie M. Schoop^{1,*}

¹*Department of Chemistry, Princeton University,
Princeton, New Jersey 08544, USA*

²*Materials Department and Materials Research Laboratory,
University of California, Santa Barbara, California 93106, USA*

³*Max-Planck-Institut für Festkörperforschung, Stuttgart, 70569, Germany*

⁴*Department of Physics, Princeton University, Princeton, NJ 08544, USA*

⁵*Argonne National Laboratory, 9700 South Cass Avenue, Argonne, IL 60439, USA*

⁶*Helmholtz-Zentrum Berlin für Materialien und Energie,
Elektronenspeicherring BESSY II, Albert-Einstein-Straße 15, 12489 Berlin, Germany*

⁷*Department of Physics and Astronomy,
Stony Brook University, Stony Brook, New York 11974, USA*

⁸*Center for Computational Quantum Physics,
The Flatiron Institute, New York, New York 10010, USA*

⁹*Donostia International Physics Center, 20018 Donostia-San Sebastian,
Spain and IKERBASQUE, Basque Foundation for Science,
Maria Diaz de Haro 3, 48013 Bilbao, Spain*

(Dated: May 27, 2022)

This PDF file includes:

Materials and Methods

Supplementary Text

Figs. S1 to S9

References

MATERIALS AND METHODS

Sample synthesis and characterization

GdSb_{0.46}Te_{1.48} single crystals were synthesized by chemical vapor transport, using iodine as the transport agent. For a detailed description of the synthesis procedure and composition characterization, see ref. (1). The crystals are typically orthogonal structurally twinned, which could obscure some details in ARPES. ARPES and X-ray photoelectron spectroscopy (XPS) experiments were performed on in-situ cleaved crystals in ultrahigh vacuum (low 10^{-10} mbar). The ARPES spectra were recorded with the 1² ARPES experiment installed at the UE112-PGM2a beam-line at the BESSY-II synchrotron, with various photon energies ranging from 60 eV to 100 eV. The core-level photoemission spectrum of GdSb_{0.46}Te_{1.48} was measured at 14 K at the 29ID-IEX beam line (Advanced Photon Source, Argonne National Laboratory) using a hemispherical Scienta R4000 electron analyzer with a pass energy of 200 eV (energy and angular resolution are 220 meV and 0.1°, respectively). Resistivity and Hall measurement were performed on plate-like single crystal samples with patterned 6-terminal gold electrodes in a Quantum Design PPMS DynaCool system. A constant AC current with an amplitude of 5 mA was applied during the measurement. Temperature-dependent DC magnetization measurements were performed via the vibrating sample magnetometer (VSM) option in the same PPMS system.

Electronic Structure Calculations

A TB-model was constructed considering p_x - and p_y -orbitals on each site, the same as that in refs. (2, 3). Hoppings between nearest-neighbor (nn) and next-nearest-neighbor (nnn) orbitals were considered. For simplification, we consider only two types of nn-hopping. One for intra-chain hopping (short bonds): $t_{spp\sigma} = 1.5$ eV and $t_{spp\pi} = -0.3$ eV, and the other for inter-chain hoppings (long bonds): $t_{lpp\sigma} = 1.3$ eV and $t_{lpp\pi} = -0.5$ eV. The nnn-hopping is simplified with one parameter: $|t_{nnn}| = 0.11$ eV. Note that this simplified treatment of the nnn-hopping does not change the symmetry of the system. The definitions of these parameters are illustrated in Fig. 1E. The TB band unfolding is achieved by projecting the band eigenstates of a supercell Hamiltonian onto that of subcell (4-6). In our result, the

intensity of the unfolded bands represent the spectral weight of each eigenstate with respect to the p_x/p_y states in the non-distorted 4^4 -net.

Density functional theory (DFT) calculations were performed in VASP *v5.4.4* (7–9) using the Perdew, Burke, Ernzerhof (PBE) functional (10). PAW potentials (11, 12) were chosen based on the *v5.2* recommendations. In order to study the role of the CDW, calculations were performed on a supercell with the experimentally-measured lattice parameters of $\text{GdSb}_{0.46}\text{Te}_{1.48}$, mimicking the true structure using the same five-fold lattice distortion along the a -axial direction. The Sb containing sites in $\text{GdSb}_{0.46}\text{Te}_{1.48}$ were modeled with full Sb occupancy, although the real structure contains partial vacancies and mixed Te occupancy as indicated in Fig. 1D. For this reason, the DFT input used a hypothetical composition of $\text{GdSb}_{0.80}\text{Te}_{1.2}$, and the resulting Fermi level is lower than that of $\text{GdSb}_{0.46}\text{Te}_{1.48}$. The Fermi level was adjusted such that it crosses the ns-DN at X, to be consistent with our experimental observation and chemical intuition.

Self-consistent calculations for the DFT subcell were found to be well converged for a plane wave energy cutoff of 500 eV and a k -mesh density, $\ell = 30$ (corresponding to $7 \times 7 \times 3$ and $1 \times 7 \times 3$ Γ -centered k -meshes for the subcell and five-fold supercell, respectively); subsequent calculations were completed using settings equal to or better than these values. Localization of the Gd f orbitals was corrected by applying a Hubbard potential $U = 6$ eV using the method of Dudarev and coworkers (13). Unfolded spectral functions for the supercell in the subcell BZ were calculated using the method of Popescu and Zunger (14) in VASPBANDUNFOLDING (15). Crystal structures were visualized with VESTA (16).

Note that both DFT subcell and supercell calculations were performed assuming a ferromagnetic (FM) order on the Gd lattice and neglecting valence spin-orbit coupling (SOC) effects. For a comparison with the experimental band structure in the paramagnetic state, we have ignored the small energy shift in the “up” and “down” spin channels, plotting only the down-spin bands. We find that SOC has almost no effect on the overall magnitude of the CDW-induced gap in the supercell calculation, although it introduces some small gaps at band-crossings and slightly shifts the relative energies of the majority and minority spin populations.

SUPPLEMENTARY TEXT

Non-symmorphic symmetry in space group $Pmmn$

Similar to ZrSiS with space group $P4/nmm$, the non-symmorphic symmetries in $\text{GdSb}_{0.46}\text{Te}_{1.48}$ in space group $Pmmn$ play important roles in protecting the four-fold (counting spin) band degeneracies, as we showed in the main text. These non-symmorphic symmetries include: the glide plane symmetry ($\widetilde{M}_z = \{M_z|\frac{1}{2}, \frac{1}{2}, 0\}$), and the two two-fold screw axes ($\widetilde{C}_{2x} = \{C_{2x}|\frac{1}{2}, 0, 0\}$, and $\widetilde{C}_{2y} = \{C_{2y}|0, \frac{1}{2}, 0\}$). In the paramagnetic state, bands are four-fold degenerate at the X, U, Y, T, S and R points, respectively. The combination of time reversal (T), inversion symmetry (P), and the glide plane symmetry (\widetilde{M}_z) protects the band degeneracy at X, U, Y and T, while the additional screw axes \widetilde{C}_{2x} and \widetilde{C}_{2y} protect the band degeneracy at X and S, and Y and S, respectively [17], as is illustrated in Fig. 1H. These symmetries also protect Dirac nodal lines (X-U,Y-T) along the BZ boundary [18].

Surface floating bands

As mentioned in the main text, surface floating bands can appear in TSMs with bulk non-symmorphic symmetry. Due to a symmetry reduction at the surface, the non-symmorphically enforced bulk band degeneracy is lifted. These surface floating bands have attracted increased attention since their discovery [18], and various interesting properties have been reported, such as high-mobility surface electronic states with an unusual protection mechanism [19], giant nonlinear optical response [20], half-missing-type anomalous Umklapp scattering in the quasiparticle interference [21], and enhanced electron-phonon coupling due to the renormalization of the surface phonon branch due to the interaction with the surface floating electrons [22]. Since $\text{GdSb}_{0.46}\text{Te}_{1.48}$ is non-symmorphic, floating bands are expected to appear. Figure S6 shows the ARPES measured surface states along $\bar{Y} - \bar{S} - \bar{Y}$, which corresponds to the $\bar{X} - \bar{M} - \bar{X}$ direction in the $P4/nmm$ space group. By comparing the DFT bulk band structure (fig. S6C) with the DFT surface band structure (fig. S6D), cone-like features of surface bands become evident: The surface bands cross the Fermi level and extend to $E_i \approx -0.6$ eV at \bar{Y} . Such features are observed in our ARPES measurements with both incident photon energies of 70 eV (fig. S6, A and B) and 100 eV (fig. S6, E and

F). As these surface states appear along the same cut as floating bands appear in ZrSiS and other square-net materials [18], we conclude that these states are also floating bands.

Extension to systems with incommensurate CDWs

Prior ARPES studies on structurally related CeTe₃ revealed that the FS around \bar{X} is unmodified by the CDW [23, 24]. The band structure of $LnTe_3$ has very small k_z dispersion and the non-symmorphic symmetry protected Dirac crossing is submerged more than 0.5 eV below the Fermi level [25], resulting in electron-pockets around \bar{X} rather than a DN at the FS. In contrast, in GdSb_{0.46}Te_{1.48} the crossing point can be at the Fermi level, and controlling the Sb/Te ratio provides the opportunity to tune the Fermi level to the desired energy. Since $LnTe_3$ ($Ln = La, Ce, Pr, Nd, Sm$ and Gd) exhibit an incommensurate CDW with varying wave vectors ranging from 0.2751 to 0.2916 r.l.u at 300 K [26], and the pocket around the \bar{X} -point is retained [4, 23–25, 27, 28], it seems that the bands at or close to \bar{X} might be immune to both incommensurate and commensurate CDW modulations.

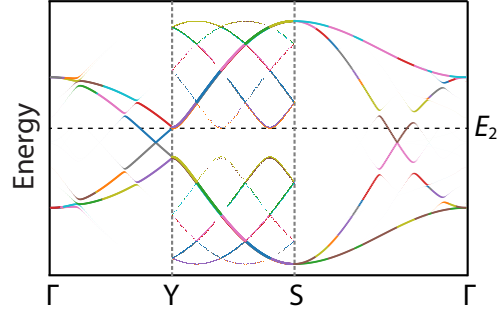


FIG. S1. Unfolded TB-band structure along Γ -Y-S- Γ .

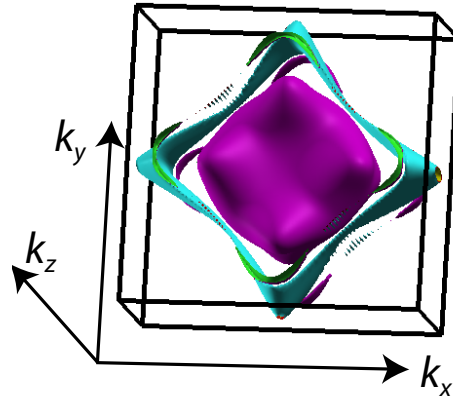


FIG. S2. Fermi surface plot of stoichiometric GdSbTe without CDW. The big purple hole-pocket centered at Γ has mainly Te p_z -character, and is highly dispersive in k_z . Visualization utilized Xcrysden[29].

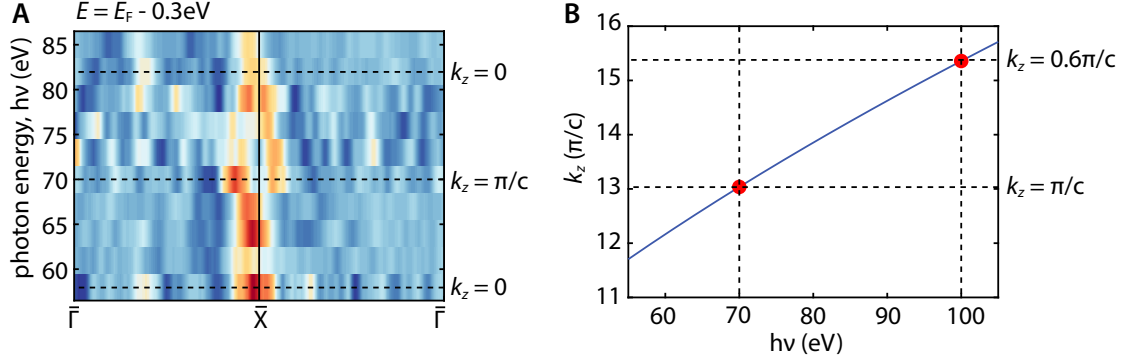


FIG. S3. Calibration of k_z by varying the photon energy in APRES. (A) Intensity plot of second derivatives of the ARPES data along $\bar{\Gamma}\text{-}\bar{X}\text{-}\bar{\Gamma}$ measured with a photon energy ranging from 58 to 85 eV, at $E = E_F - 0.3$ eV. (B) Photon energy dependent k_z after calibration. Incident photon energies of 70 and 100 eV correspond to $k_z = \pi/c$ and $k_z = 0.6\pi/c$, respectively.

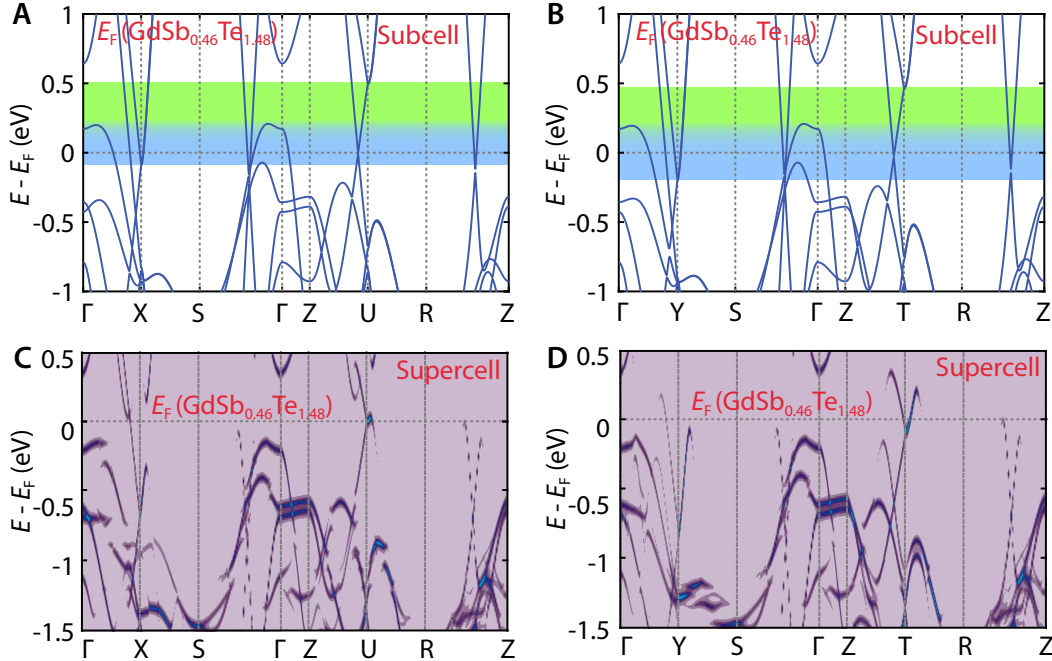


FIG. S4. Comparison of DFT-calculated band structure of the subcell and the supercell. (A and B) Band structures of GdSbTe along $\Gamma\text{-X-S-}\Gamma\text{-Z-U-R-Z}$ and $\Gamma\text{-Y-S-}\Gamma\text{-Z-T-R-Z}$, respectively. The color-shaded regions indicate the energy span of the nodal lines along X-U and Y-T in (A) and (B), respectively, in accordance with Fig. 1I. (C and D) Unfolded band structures of the five-fold supercell along $\Gamma\text{-X-S-}\Gamma\text{-Z-U-R-Z}$ and $\Gamma\text{-Y-S-}\Gamma\text{-Z-T-R-Z}$, respectively.

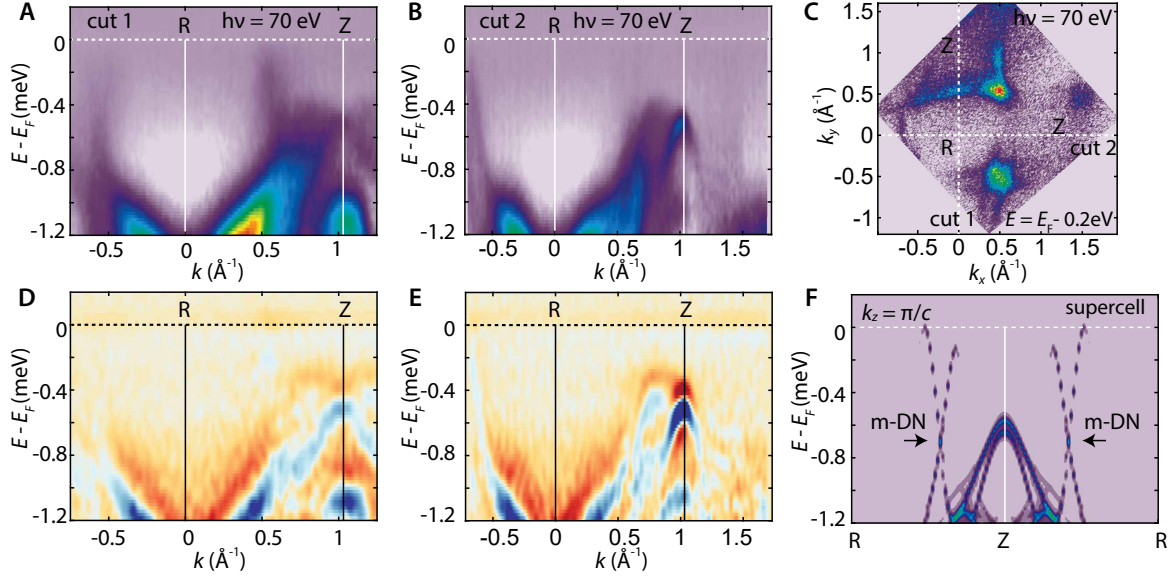


FIG. S5. ARPES band dispersion along R-Z-R ($k_z = \pi/c$ plane) in comparison to DFT. (A and B) ARPES band dispersion along two orthogonal Z-R-Z directions. (C) Illustration of the k -paths for the two band-dispersion cuts shown in (A) and (B). (D and E) Laplacian plots of (A) and (B), respectively. (F) The unfolded band dispersion from supercell DFT calculation.

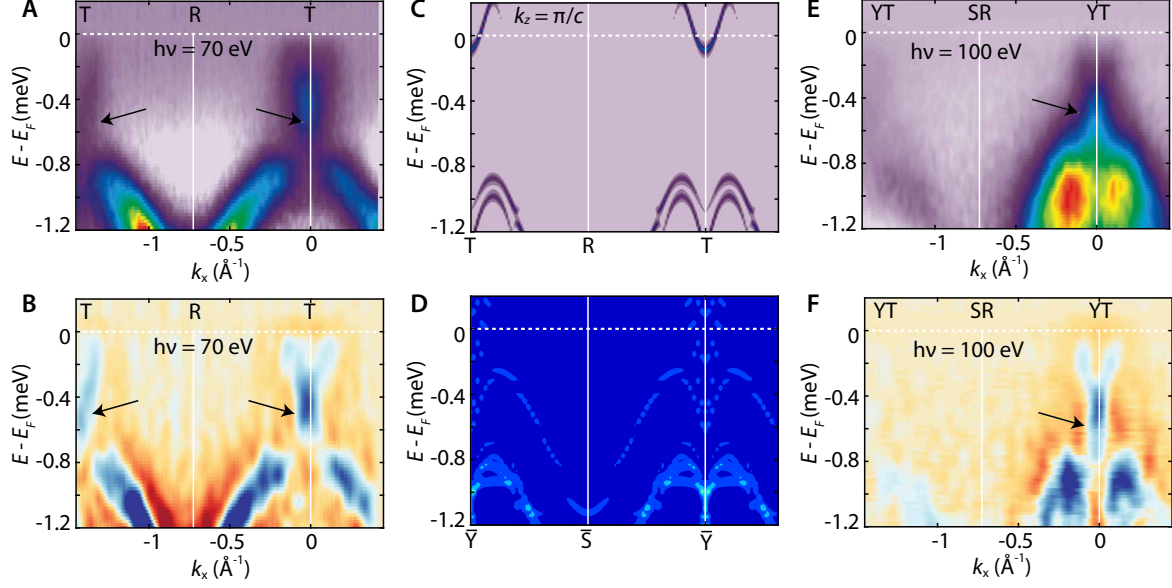


FIG. S6. Observations of surface floating bands in $\text{GdSb}_{0.46}\text{Te}_{1.48}$. (A and B) ARPES band structure and its Laplacian along T-R-T path ($k_z = \pi/c$ plane), with an incident photon energy of $h\nu = 70$ eV. (C) The unfolded band dispersion along T-R-T from bulk DFT supercell calculation. (D) The unfolded band dispersion along $\bar{Y} - \bar{S} - \bar{Y}$ from a surface DFT supercell calculation. (E and F) ARPES band structure and its Laplacian along YT-SR-YT path ($k_z = 0.6\pi/c$ plane), with an incident photon energy of $h\nu = 100$ eV. Arrows in (A), (B), (E) and (F) indicate the surface floating bands.

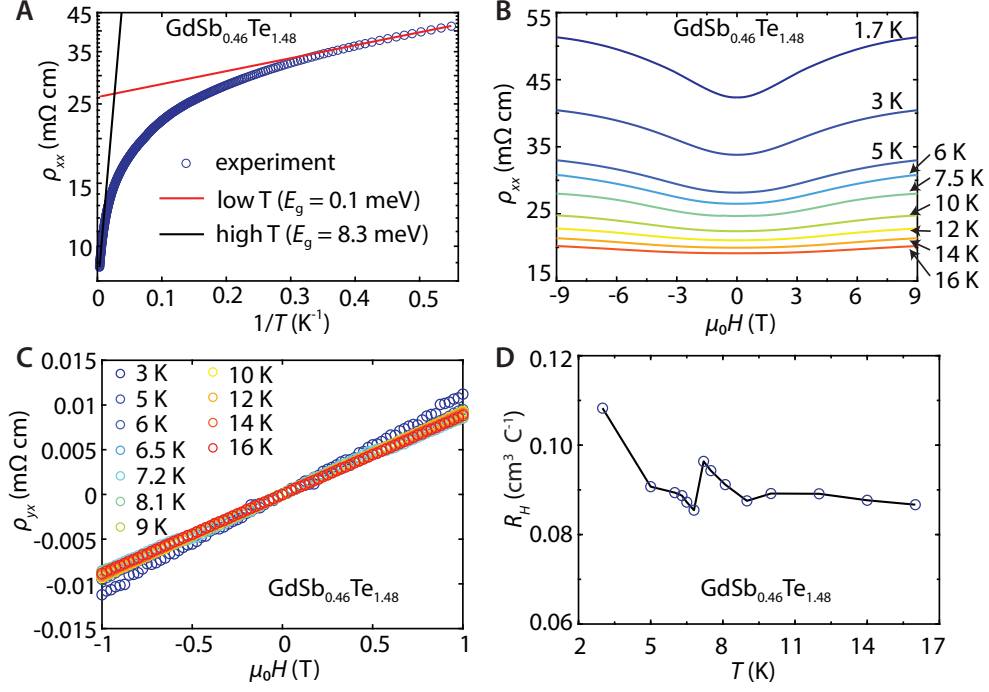


FIG. S7. Transport measurement of $\text{GdSb}_{0.46}\text{Te}_{1.48}$. (A) Temperature dependent resistivity, plotted in a log vs $1/T$ scale. The fits were performed assuming a local Arrhenius-type $\rho \sim \exp(E_g/2k_B T)$ relation. k_B is the Boltzmann constant. The low-temperature (low T) fit was performed for $1.8 \text{ K} < T < 10 \text{ K}$, and the high-temperature (high T) fit was performed for $290 \text{ K} < T < 300 \text{ K}$. (B) Magnetoresistance measured at several different temperatures. (C) Hall resistivity measured at several different temperatures. (D) Temperature dependent Hall coefficients extracted from (C) at the field of 0.5 T. The Hall coefficient is mostly T -independent. Note that the lines are drawn to guide the eye.

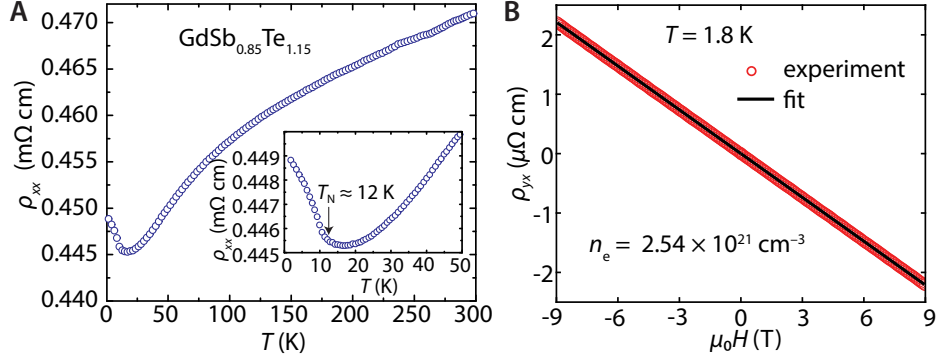


FIG. S8. Resistivity and Hall measurement of tetragonal $\text{GdSb}_{0.85}\text{Te}_{1.15}$. (A) Temperature dependent resistivity. Inset shows a zoom-in view at low temperature. The Néel temperature is $T_N \approx 12$ K ($T_N = 11.5$ K inferred from DC magnetic susceptibility measurement). (B) Hall measurement shows a linear field dependence with a negative slope, suggesting electrons as the dominant carrier type in this system. The carrier concentration is $n_e = 2.54 \times 10^{21} \text{ cm}^{-3}$.

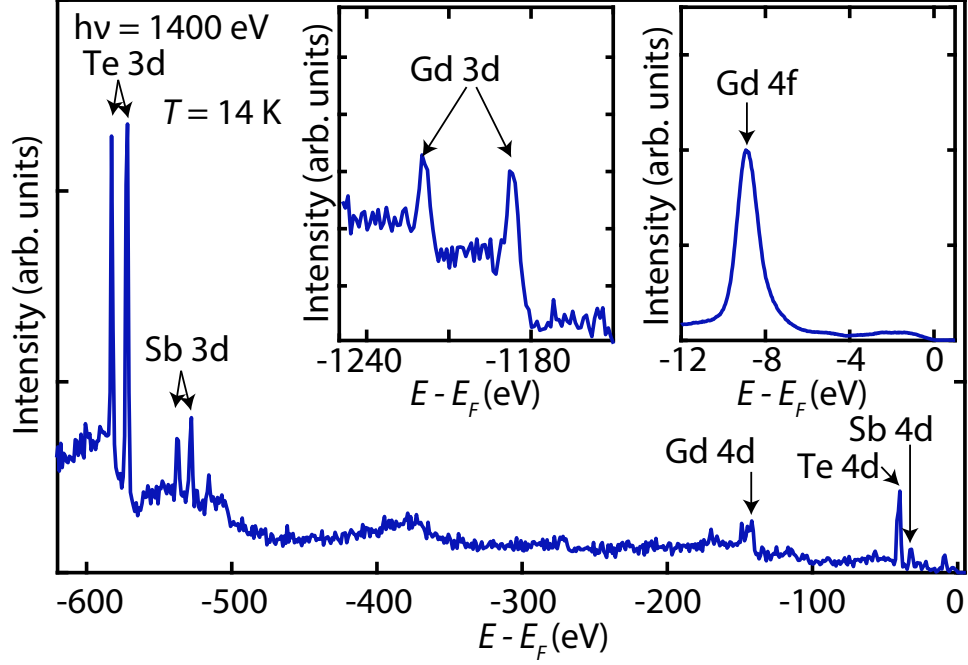


FIG. S9. Core level photoemission spectrum measured with an incident photon energy of $h\nu = 1400$ eV at 14 K. It reveals the characteristic peaks coming from Sb $3d$, Sb $4d$, Te $3d$, Te $4d$, Gd $3d$, Gd $4d$ and Gd $4f$ states, while the oxygen peak is absent, demonstrating the good quality of the sample after cleavage. Insets show the low binding-energy peak of Gd $4f$ states, and high binding-energy peaks of Gd $3d$ states, respectively. The Gd $4f$ states are centered at 8.9 eV below the Fermi level with a FWHM (full width at half maximum) width of 1.3 eV.

* lschoop@princeton.edu

- [1] S. Lei, V. Duppel, J. M. Lippmann, J. Nuss, B. V. Lotsch, and L. M. Schoop, *Advanced Quantum Technologies* **2**, 1900045 (2019).
- [2] S. Klemenz, L. Schoop, and J. Cano, *Phys. Rev. B* **101**, 165121 (2020).
- [3] S. Klemenz, A. K. Hay, S. M. L. Teicher, A. Topp, J. Cano, and L. M. Schoop, *Journal of the American Chemical Society* **142**, 6350 (2020).
- [4] E. Lee, D. H. Kim, H. W. Kim, J. D. Denlinger, H. Kim, J. Kim, K. Kim, B. I. Min, B. H. Min, Y. S. Kwon, and J.-S. Kang *Scientific Reports* **6**, 30318 (2016).
- [5] T. B. Boykin and G. Klimeck, *Physical Review B* **71**, 115215 (2005).
- [6] W. Ku, T. Berlijn, and C.-C. Lee, *Physical Review Letters* **104**, 216401 (2010).
- [7] G. Kresse and J. Hafner, *Phys. Rev. B* **49**, 14251 (1994).
- [8] G. Kresse and J. Furthmüller, *Phys. Rev. B* **54**, 11169 (1996).
- [9] G. Kresse and J. Furthmüller, *Comput. Mater. Sci.* **6**, 15 (1996).
- [10] J. P. Perdew, K. Burke, and M. Ernzerhof, *Phys. Rev. Lett.* **77**, 3865 (1996).
- [11] P. E. Blöchl, *Phys. Rev. B* **50**, 17953 (1994).
- [12] G. Kresse and D. Joubert, *Phys. Rev. B* **59**, 1758 (1999).
- [13] S. L. Dudarev, G. A. Botton, S. Y. Savrasov, C. J. Humphreys, and A. P. Sutton, *Phys. Rev. B* **57**, 1505 (1998).
- [14] V. Popescu and A. Zunger, *Phys. Rev. B* **85**, 085201 (2012).
- [15] Q. Zheng, “Vasp band unfolding,” <https://github.com/QijingZheng/VaspBandUnfolding>.
- [16] K. Momma and F. Izumi, *J. Appl. Crystallogr.* **44**, 1272 (2011).
- [17] S. M. Young and C. L. Kane, *Phys. Rev. Lett.* **115**, 126803 (2015).
- [18] A. Topp, R. Queiroz, A. Grüneis, L. MÜchler, A. Rost, A. Varykhalov, D. Marchenko, M. Krivenkov, F. Rodolakis, J. Mc-Chesney, L. B. V, S. L. M, and C. R. Ast, *Phys. Rev. X* **7**, 041073 (2017).
- [19] X. Liu, C. Yue, Y. Zhu, A. Joshy, J. Liu, A. M. Sanchez, D. Graf, Z. Mao, J. Hu, and J. Wei, *arXiv:1911.06799* (2019).
- [20] S. Chi, F. Liang, H. Chen, W. Tian, H. Zhang, H. Yu, G. Wang, Z. Lin, J. Hu, and H. Zhang, *Advanced Materials* **32**, 1904498 (2019).

- [21] Z. Zhu, T.-R. Chang, C.-Y. Huang, H. Pan, X.-A. Nie, X.-Z. Wang, Z.-T. Jin, S.-Y. Xu, S.-M. Huang, D.-D. Guan, S. Wang, Y.-Y. Li, C. Liu, D. Qian, W. Ku, F. Song, H. Lin, H. Zheng, and J.-F. Jia. *Nature Communications* **9**, 1 (2018).
- [22] S. Xue, T. Zhang, C. Yi, S. Zhang, X. Jia, L. H. Santos, C. Fang, Y. Shi, X. Zhu, and J. Guo, *Physical Review B* **100**, 195409 (2019).
- [23] V. Brouet, W. Yang, X. Zhou, Z. Hussain, N. Ru, K. Shin, I. Fisher, and Z. Shen, *Physical Review Letters* **93**, 126405(2004).
- [24] V. Brouet, W. Yang, X. Zhou, Z. Hussain, R. Moore, R. He, D. Lu, Z. Shen, J. Laverock, S. Dugdale, N. Ru, and I. R. Fisher, *Physical Review B* **77**, 235104 (2008).
- [25] S. Lei, J. Lin, Y. Jia, M. Gray, A. Topp, G. Farahi, S. Klemenz, T. Gao, F. Rodolakis, J. L. McChesney, C. R. Ast, A. Yazdani, K. S. Burch, S. Wu, N. P. Ong, and L. M. Schoop, *Science Advances* **6**, eaay6407 (2020).
- [26] C. D. Malliakas and M. G. Kanatzidis, *J. Am. Chem. Soc.* **128**, 12612 (2006).
- [27] G. H. Gweon, J. D. Denlinger, J. A. Clack, J. W. Allen, C. G. Olson, E. DiMasi, M. C. Aronson, B. Foran, and S. Lee, *Phys. Rev. Lett.* **81**, 886 (1998)
- [28] N. Ru, R. Borzi, A. Rost, A. Mackenzie, J. Laverock, S. Dugdale, and I. Fisher, *Physical Review B* **78**, 045123 (2008).
- [29] A. Kokalj, *Journal of Molecular Graphics and Modelling* **17**, 176 (1999).